The reduction of plankton biomass induced by mesoscale stirring: a modelling study in the Benguela upwelling.

Ismael Hernández-Carrasco[a,*], Vincent Rossi[a,b], Emilio Hernández-García[a], Veronique Garçon[b], Cristóbal López[a]

[a] *IFISC, Instituto de Física Interdisciplinar y Sistemas Complejos (CSIC-UIB), 07122 Palma de Mallorca, Spain*
[b] *Laboratoire d'Études en Géophysique et Océanographie Spatiale, CNRS, Observatoire Midi-Pyrénées, 14 avenue Edouard Belin, Toulouse, 31401 Cedex 9, France*

Abstract

Recent studies, both based on remote sensed data and coupled models, showed a reduction of biological productivity due to vigorous horizontal stirring in upwelling areas. In order to better understand this phenomenon, we consider a system of oceanic flow from the Benguela area coupled with a simple biogeochemical model of Nutrient-Phyto-Zooplankton (NPZ) type. For the flow three different surface velocity fields are considered: one derived from satellite altimetry data, and the other two from a regional numerical model at two different spatial resolutions. We compute horizontal particle dispersion in terms of Lyapunov Exponents, and analyzed their correlations with phytoplankton concentrations. Our modelling approach confirms that in the south Benguela there is a reduction of biological activity when stirring is increased. Two-dimensional offshore advection and latitudinal difference in Primary Production, also mediated by the flow, seem to be the dominant processes involved. We estimate that mesoscale processes are responsible for 30 to 50% of the offshore fluxes of biological tracers. In the northern area, other factors not taken into account in our simulation are influencing the ecosystem. We suggest explanations for these results in the context of studies performed in other eastern boundary upwelling areas.

*Corresponding author. Tel.: +34 971 172668
Email address: ismael@ifisc.uib-csic.es (Ismael Hernández-Carrasco)

1. Introduction

Marine ecosystems of the Eastern Boundary Upwelling zones are well known for their major contribution to the world ocean productivity. They are characterized by wind-driven upwelling of cold nutrient-rich waters along the coast that supports elevated plankton and pelagic fish production (Mackas et al., 2006). Variability is introduced by strong advection along the shore, physical forcings by local and large scales winds, and high submeso- and meso-scale activities over the continental shelf and beyond, linking the coastal domain with the open ocean.

The Benguela Upwelling System (BUS) is one of the four major Eastern Boundary Upwelling Systems (EBUS) of the world. The coastal area of the Benguela ecosystem extends from southern Angola (around 17°S) along the west coast of Namibia and South Africa (36°S). It is surrounded by two boundary currents, the warm Angola Current in the north, and the temperate Agulhas Current in the south. The BUS can itself be subdivided into two subdomains by the powerful Luderitz upwelling cell (Hutchings et al., 2009). Most of the biogeochemical activity occurs within the upwelling front and the coast, although it can be extended further offshore toward the open ocean by the numerous filamental structures developing offshore (Monteiro, 2009). In the BUS, as in the other major upwelling areas, high mesoscale activity due to eddies and filaments impacts strongly marine planktonic ecosystem over the continental shelf and beyond (Brink and Cowles, 1991; Martin, 2003; Sandulescu et al., 2008; Rossi et al., 2009).

The purpose of this study is to analyze the impact of horizontal stirring on phytoplankton dynamics in the BUS within an idealized two dimensional modelling framework. Based on satellite data of the ocean surface, Rossi et al. (2008, 2009) recently suggested that mesoscale activity has a negative effect on chlorophyll standing stocks in the four EBUS. This was obtained by correlating remote sensed chlorophyll data with a Lagrangian measurement of lateral stirring in the surface ocean (see Methods section). This result was unexpected since mesoscale physical structures, particularly mesoscale eddies, have

been related to higher planktonic production and stocks in the open ocean (McGillicuddy et al., 2007) as well as off a major EBUS (Correa-Ramirez et al., 2007). A more recent and thorough study performed by Gruber et al. (2011) in the California and the Canary current systems extended the initial results from Rossi et al. (2008, 2009). Based on satellite derived estimates of net Primary Production, of upwelling strength and of Eddy Kinetic Energy (EKE) as a measure the intensity of mesoscale activity, they confirmed the suppressive effect of mesoscale structures on biological production in upwelling areas. Investigating the mechanism behind this observation by means of on 3D eddy-resolving coupled models, Gruber et al. (2011) showed that mesoscale eddies tend to export offshore and downward a certain pool of nutrients not being effectively used by the biology in the coastal areas. This process they called "nutrients leakage" is also having a negative feedback by diminishing the pool of deep nutrients available in the surface waters being re-upwelled continuously.

In our work, we focused on the Benguela area, being the most contrasting area of all EBUS in terms of stirring intensity (Rossi et al., 2009). Although the mechanisms studied by Gruber et al. (2011) seem to involve 3D dynamics, the initial observation of this suppressive effect was essentially based on two-dimensional (2D) datasets (Rossi et al., 2008). In this work we use 2D numerical analysis in a semi-realistic framework to better understand the effects of a 2D turbulent flow on biological dynamics, apart from the complex 3D bio-physical processes. The choice of this simple horizontal numerical approach is indeed supported by other theoretical 2D studies that also displayed a negative correlation between stirring and biomass (Tél et al., 2005; MacKiver and Neufeld, 2009; Neufeld and Hernández-García, 2009). Meanwhile, since biological productivity in upwelling areas rely on the (wind-driven) vertical uplift of nutrients, we introduced in our model a nutrient source term with an intensity and spatial distribution corresponding to the upwelling characteristics. Instead of the commonly used EKE, which is an Eulerian diagnostic tool, we used here a Lagrangian measurement of mesoscale stirring that has been

demonstrated as a powerful tool to study patchy chlorophyll distributions influenced by dynamical structures at mesoscale, such as upwelling filaments (Calil and Richards, 2010). The Lagrangian perspective provides a complementary insight to transport phenomena in the ocean with respect to the Eulerian one. In particular, the concept of Lagrangian Coherent Structure may give a global idea of transport in a given area, separating regions with different dynamical behavior, and signaling avenues and barriers to transport, which are of great relevance for the marine biological dynamics. While the Eulerian approach describes the characteristics of the velocity field, the Lagrangian one addresses the effects of this field on transported substances, which is clearly more directly related to the biological dynamics. For example the work by Hernández-Carrasco et al. (2012) describes currents in the world ocean having the same level of Eddy Kinetic Energy but having two different stirring characteristics, as quantified by Lagrangian tools. Further discussions comparing Lagrangian and Eulerian diagnostics can be found, for example, in d'Ovidio et al. (2009) and the above cited Hernández-Carrasco et al. (2012). To consider velocity fields with different characteristics and to test the effect of the spatial resolution, different flow fields are used, one derived from satellite and two produced by numerical simulations at two different spatial resolutions. Our modelled chlorophyll-a concentrations are compared with observed distributions of chlorophyll-a (a metric for phytoplankton) obtained from the SeaWiFS satellite sensor.

This paper is organized as follows. Sec. 2 is a brief description of the different datasets used in this study. Sec. 3 depicts the methodology, which includes the computation of the finite-size Lyapunov exponents, and the numerical plankton-flow 2D coupled model. Then, our results are analyzed and discussed in Sec. 4. Finally in Sec. 5, we summed-up our main findings.

2. Satellite and simulated data

We used three different 2D surface velocity fields of the Benguela area. Two are obtained from the numerical model Regional Ocean Model System (ROMS), and the other one from a combined satellite product.

2.1. Surface velocity fields derived from regional simulations.

ROMS is a free surface, hydrostatic, primitive equation model, and we used here an eddy-resolving climatologically forced run provided by (Gutknecht et al., 2013). At each grid point, linear horizontal resolution is the same in both the longitudinal, ϕ, and latitudinal, θ, directions, which leads to angular resolutions $\Delta\phi = \Delta_0$ and $\Delta\theta = \Delta\phi \cos\theta$. The numerical model was run onto 2 different grids: a coarse one at spatial resolution of $\Delta_0 = 1/4°$, and a finer one at $\Delta_0 = 1/12°$ of spatial resolution. In the following we label the dataset from the coarser resolution run as *ROMS1/4*, and the finer one as *ROMS1/12*. For both runs, vertical resolution is variable with 30 layers in total, while only data from the surface upper layer are used in the following. Since the flows are obtained from climatological forcings, they would represent a mean annual cycle of the typical surface currents of the Benguela region.

2.2. Surface velocity field derived from satellite

A velocity field derived from satellite observations is compared to the simulated fields described previously. It consists of surface currents computed from a combination of wind-driven Ekman currents, at 15 m depth, derived from Quickscat wind estimates, and geostrophic currents calculated using time-variable Sea Surface Heights (SSH) obtained from satellite (Sudre and Morrow, 2008). These SSH were calculated from mapped altimetric sea level anomalies combined with a mean dynamic topography. This velocity field, labeled as *Satellite1/4*, covers a period from June 2002 to June 2005 with a spatial resolution of $\Delta_0 = 1/4°$ in both longitudinal and latitudinal directions.

2.3. Ocean color as a proxy for phytoplankton biomass

To validate simulated plankton concentrations, we use a three-year-long time series, from January 2002 to January 2005, of ocean color data. Phytoplankton pigment concentration (chlorophyll-a) is obtained from monthly Sea viewing Wide Field-of-view Sensor (SeaWiFS) products, generated by the NASA Goddard Earth Science (GES)/Distributed Active Archive Center (DAAC). Gridded global data were used with a resolution of approximately 9 by 9 km.

3. Methodology

3.1. Finite-Size Lyapunov Exponents (FSLEs)

FSLEs (Artale et al., 1997; Aurell et al., 1997; Boffetta et al., 2001) provides a measure of dispersion, and thus of stirring and mixing, as a function of the spatial resolution. This Lagrangian tool allows isolating the different regimes corresponding to different length scales of the oceanic flows, as well as identifying Lagrangian Coherent Structures (LCSs) present in the data (Tew Kai et al., 2009). FSLE are computed from τ, the time required for two particles of fluid (one of them placed at $\mathbf{x}$) to separate from an initial distance of δ_0 (at time t) to a final distance of δ_f, as

$$\lambda(\mathbf{x}, t, \delta_0, \delta_f) = \frac{1}{\tau} \log \frac{\delta_f}{\delta_0}. \tag{1}$$

It is natural to choose the initial points $\mathbf{x}$ on the nodes of a grid with lattice spacing coinciding with the initial separation of fluid particles δ_0. Then, values of λ are obtained in a grid with lattice separation δ_0. In most of this work the resolution of the FSLE field, δ_0, is chosen equal to the resolution of the velocity field, Δ_0. Other choices of parameter are possible and δ_0 can take any value, even much smaller than the resolution of the velocity field (Hernández-Carrasco et al., 2011). This opens many possibilities that will not be fully explored in this work (see also Fig. 3 and Appendix A.1) . Using similar parameters for the FSLEs' computation, We also investigate the response of the coupled

biophysical system to variable resolution of the velocity field, (see Hernández-Carrasco et al. (2011) for further details about the sensitivity and robustness of the FSLEs).

The field of FSLEs thus depends on the choice of two length scales: the initial, δ_0 and the final δ_f separations. As in previous works (d'Ovidio et al., 2004, 2009; Hernández-Carrasco et al., 2011) we focus on transport processes at mesoscale, so that δ_f is taken as about 110 km, or 1°, which is the order of the size of mesoscale eddies at mid latitudes. To compute λ we need to know the trajectories of the particles, which gives the Lagrangian character to this quantity. The equations of motion that describe the horizontal evolution of particle trajectories in longitudinal and latitudinal spherical coordinates, $\mathbf{x} = (\phi, \theta)$, are:

$$\frac{d\phi}{dt} = \frac{u(\phi,\theta,t)}{R\cos\theta}, \tag{2}$$

$$\frac{d\theta}{dt} = \frac{v(\phi,\theta,t)}{R}, \tag{3}$$

where u and v represent the eastwards and northwards components of the surface velocity field, and R is the radius of the Earth (6371 km).

The ridges of the FSLE field can be used to define the Lagrangian Coherent Structures (LCSs) (Haller and Yuan, 2000; d'Ovidio et al., 2004, 2009; Tew Kai et al., 2009; Hernández-Carrasco et al., 2011), which are useful to characterize the flow from the Lagrangian point of view (Joseph and Legras, 2002; Koh and Legras, 2002). Since we are only interested in the ridges of large FSLE values, the ones which significantly affect stirring, LCSs can be computed by the high values of FSLE which have a line-like shape. We compute FSLEs by integrating backwards-in-time the particle trajectories since attracting LCSs (and its associated unstable manifolds) have a direct physical interpretation (Joseph and Legras, 2002; d'Ovidio et al., 2004, 2009). Tracers, such as temperature and chlorophyll-a, spread along the attracting LCSs, thus creating their typical filamental structure (Lehan et al., 2007; Calil and Richards, 2010).

3.2. The Biological model

The plankton model is similar to the one used in previous studies by Oschlies and Garçon (1998, 1999) and Sandulescu et al. (2007, 2008). It describes the interaction of a three-level trophic chain in the mixed layer of the ocean, including phytoplankton P, zoo-plankton Z and dissolved inorganic nutrient N, whose concentrations evolve in time according to the following equations:

$$\frac{dN}{dt} = F_N = \Phi_N - \beta \frac{N}{\kappa_N + N} P + \mu_N \left((1-\gamma) \frac{\alpha \eta P^2}{\alpha + \eta P^2} Z + \mu_P P + \mu_z Z^2 \right), \tag{4}$$

$$\frac{dP}{dt} = F_P = \beta \frac{N}{\kappa_N + N} P - \frac{\alpha \eta P^2}{\alpha + \eta P^2} Z - \mu_P P, \tag{5}$$

$$\frac{dZ}{dt} = F_Z = \gamma \frac{\alpha \eta P^2}{\alpha + \eta P^2} Z - \mu_Z Z^2, \tag{6}$$

where the dynamics of the nutrients, Eq. (4), is determined by nutrient supply due to the vertical transport Φ_N, its uptake by phytoplankton (2^{nd} term) and its recycling by bacteria from sinking particles (remineralization) (3^{rd} term). Vertical mixing which brings subsurface nutrients into the mixed surface layer of the ocean is parameterized in our coupled model (see below), since the hydrodynamical part considers only horizontal 2D transport. The terms in Eq. (5) represent the phytoplankton growth by consumption of N (i.e. primary production $PP = \frac{N}{\kappa_N + N} P$), the grazing by zooplankton ($G_z = \frac{\alpha \eta P^2}{\alpha + \eta P^2} Z$), and natural mortality of phytoplankton. The last equation, Eq. (6), represents zooplankton growth by consuming phytoplankton minus zooplankton quadratic mortality.

An important term of our model is the parameterization of the vertical transport of nutrients by coastal upwelling. Assuming constant nutrient concentration N_b below the mixed layer, this term can be expressed as:

$$\Phi_N(\mathbf{x}, t) = S(\mathbf{x}, t)(N_b - N(\mathbf{x}, t)), \tag{7}$$

where the function S, which depends on time and space (on the two dimensional location $\mathbf{x}$), determines the amplitude and the spatial distribution of vertical mixing in the model,

thus specifying the strength of the coastal upwelling. Thus, the function S represents the vertical transport due to coastal upwelling in our 2D model. Upwelling intensity along the coast is characterized by a number of coastal cells of enhanced vertical Ekman driven transport that are associated with similar fluctuations of the alongshore wind (Demarcq et al., 2003; Veitch et al., 2009). Following these results, we defined our function S as being null over the whole domain except in a 0.5° wide coastal strip, varying in intensity depending on the latitude concerned (see Fig. 1). Six separate upwelling cells, peaking at approximately 33°S, 31°S, 27.5°S, 24.5°S, 21.5°S, 17.5°S,can be discerned. They are named Cape Peninsula, Columbine/Namaqua, Luderitz, Walvis Bay, Namibia and Cunene, respectively, Luderitz being the strongest. For the temporal dependence, S switches between a summer and a winter parameterization displayed in Fig. 1.

When Φ_N is fixed to either its summer or its winter shape described in Fig. 1, the dynamical system given by Eqs. (4,5,6) evolves towards an equilibrium distribution for N, P and Z. The transient time to reach equilibrium is typically 60 days with the initial concentrations used (see Sec. 3.3). The parameters are set following a study by Pasquero et al. (2004) and are listed in Table 1.

3.3. Coupling hydrodynamical and biological models in Benguela.

We used the velocity fields provided by (Sudre and Morrow, 2008) and (Gutknecht et al., 2013) to do offline coupling with the NPZ model. The evolution of simulated concentrations advected within a flow is determined by the coupling between the hydrodynamical and biological models, as described by an advection-reaction-diffusion system. The complete model is given by the following system of partial differential equations:

$$\frac{\partial N}{\partial t} + \mathbf{v} \cdot \nabla N = F_N + D\nabla^2 N, \tag{8}$$

$$\frac{\partial P}{\partial t} + \mathbf{v} \cdot \nabla P = F_P + D\nabla^2 P, \tag{9}$$

$$\frac{\partial Z}{\partial t} + \mathbf{v} \cdot \nabla Z = F_Z + D\nabla^2 Z. \tag{10}$$

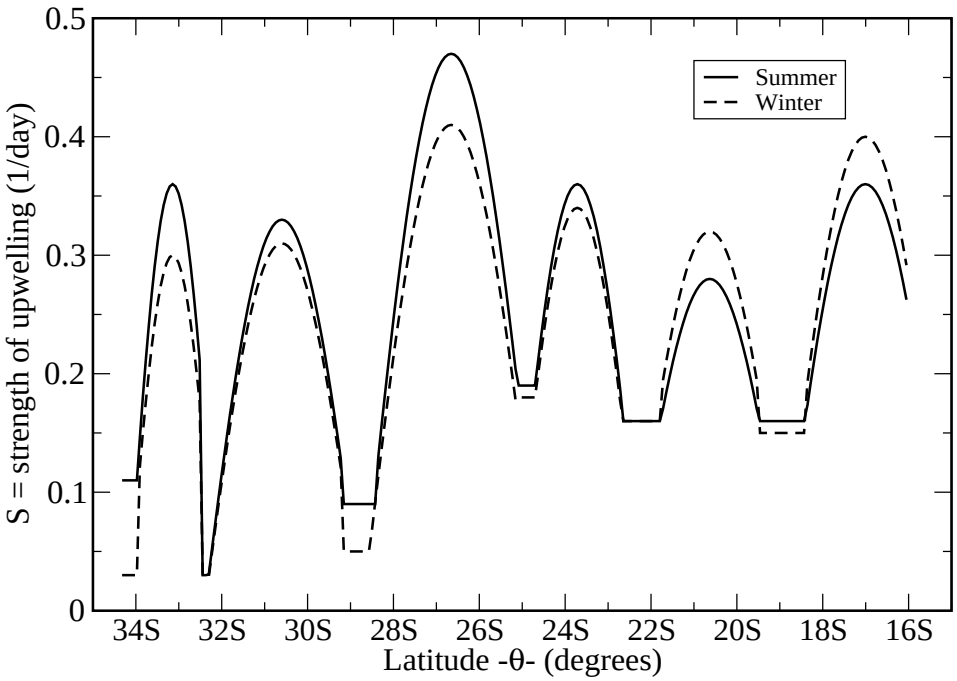

Figure 1: Shape and values of the strength (S) of the upwelling cells used in the simulations for winter and summer seasons (following Veitch et al. (2009)).

The biological model is the one described previously by the functions F_N, F_P and F_Z. Horizontal advection is the 2D velocity field $\mathbf{v}$, which is obtained from satellite data or from the ROMS model. We add also an eddy diffusion term, via the ∇^2 operator, acting on N, P, and Z to incorporate the unresolved small-scales which are not explicitly taken into account by the velocity fields used.

The eddy diffusion coefficient, D, is given by Okubo's formula (Okubo, 1971), $D(l) = 2.055 * 10^{-4}\ l^{1.15}$, where l is the value of the resolution, in meters, corresponding to the angular resolution $l = \Delta_0$. The formula gives the values D=26.73 m^2/s for *Satellite1/4* and *ROMS1/4*, and D=7.4 m^2/s for *ROMS1/12*.

Parameter	Symbol	Value
Phytoplankton growth rate	β	0.66 day^{-1}
Prey capture rate	η	1.0 (mmol N m^{-3})$^{-2}$ day^{-1}
Assimilation efficiency of Zooplankton	γ	0.75
Maximum grazing rate	a	2.0 day^{-1}
Half-saturation constant for N uptake	k_N	0.5 mmol N m^{-3}
Inefficiency of remineralization	μ_N	0.2
Specific mortality rate	μ_P	0.03 day^{-1}
(Quadratic) mortality	μ_Z	0.2 (mmol N m^{-3})$^{-1}$ day^{-1}
Nutrient concentration bellow mixed layer	N_b	8.0 mmol N m^{-3}

Table 1: List of parameters used in the biological model.

The coupled system Eqs. (8),(9) and (10) is solved numerically by the semi-Lagrangian algorithm described in Sandulescu et al. (2007), combining Eulerian and Lagrangian schemes. The initial concentrations of the tracers were taken from Koné et al. (2005) and they are $N_0 = 1\ mmolNm^{-3}$, $P_0 = 0.1\ mmolNm^{-3}$, and $Z_0 = 0.06\ mmolNm^{-3}$. The inflow conditions at the boundaries are specified in the following way: at the eastern corner, and at the western and southern edges of the computational domain fluid parcels enter with very low concentrations ($N_L = 0.01N_0\ mmolNm^{-3}$, $P_L = 0.01P_0\ mmolNm^{-3}$, and $Z_L = 0.01Z_0\ mmolNm^{-3}$). Across the northern boundary, fluid parcels enter with higher concentrations ($N_H = 5\ mmolNm^{-3}$, $P_H = 0.1\ mmolNm^{-3}$, and $Z_H = 0.06\ mmolNm^{-3}$). Nitrate concentrations are derived from CARS climatology (Condie and Dunn, 2006), while P and Z concentrations are taken from Koné et al. (2005). The integration time step is $dt = 6$ hours.

To convert the modeled P values, originally in $mmolN.m^{-}3$, into $mg\ m^{-3}$ of chlorophyll, we used a standard ratio of $Chloro/Nitrogen = 1.59$ as prescribed by Hurtt and Armstrong (1996) and Doney (1996). In the following we refer to as "simulated chloro-

phyll" for the concentrations derived from the simulated phytoplankton P, after applying the conversion ratio (see above); and we use "observed chlorophyll" for the chlorophyll-a measured by SeaWIFS.

4. Results and discussion

4.1. Validation of our simple 2D idealized setting using satellite data

4.1.1. Horizontal stirring

We compute the FSLE with an initial separation of particles equal to the spatial resolution of each velocity field ($\delta_0 = 1/4^\circ$ for *Satellite1/4* and *ROMS1/4*, and $\delta_0 = 1/12^\circ$ for *ROMS1/12*), an a final distance of $\delta_f = 1^\circ$ to focus on transport processes by mesoscale structures at mid latitudes. The areas of more intense horizontal stirring due to mesoscale activity can be identified by large values of temporal averages of backward FSLEs (see Figure 2). While there are visible differences between the results from the different velocity fields, especially in the small-scale patterns, the spatial pattern are quantitatively well reproduced. For instance, spatial correlation coefficient R^2 between FSLEs map from *Satellite1/4* and from *ROMS1/4* is 0.81. Correlation coefficients between *Satellite1/4* and *ROMS1/12* on one hand, and between *ROMS1/4* and *ROMS1/12* on the other hand, are lower (0.61 and 0.77 respectively) since the FSLE were computed on a different resolution. More details on the effect on the grid resolution when computing FSLEs can be found in Hernández-Carrasco et al. (2011). For all datasets, high stirring values are observed in the southern region, while the northern area displays significantly lower values, in line with Rossi et al. (2009). Note that the separation is well marked for *Satellite1/4* where high and low values of FSLE occur below and above a line at 27° approximately. In the case of ROMS flow fields, the stirring activity is more homogeneously distributed, although the north-south gradient is still present. We associate this latitudinal gradient with the injection of energetic Agulhas rings, the intense jet/bathymetry interactions and with other source of flow instabilities in the southern Benguela. Following Gruber

et al. (2011) we compute the EKE, another proxy of the intensity of mesoscale activity. There are regions with distinct dynamical characteristics as the southern subsystem is characterized by larger EKE values than the northern area, in good agreement with the analysis arising from FSLEs (Fig. 2). Spatial correlations (not shown) indicate that EKE and FSLE patterns are well correlated using a non-linear fitting (power law). For instance, EKE and FSLE computed on the velocity field from *Satellite1/4* exhibit a R^2 of 0.86 for the non-linear fitting: $FSLE = 0.009 \cdot EKE^{0.49}$. This is in agreement with the initial results from Waugh et al. (2006); Waugh and Abraham (2008), for a related dispersion measurement, and confirmed for the Benguela region by the thorough investigations of EKE/FSLE relationship by Hernández-Carrasco et al. (2012).

To analyze the variability of horizontal mixing with latitude, we compute longitudinal averages of the plots in Fig. 2 for two different coastally-oriented strips extended: a) from the coast to 3° offshore, and b) from 3° to 6° offshore (see Fig. 3). It allows analyzing separately subareas characterized by distinct bio-physical characteristics (see also Rossi et al. (2009)), the coastal upwelling (3° strip) with high plankton biomasses and moderated mesoscale activity, and the open ocean (from 3° to 6° offshore) with moderated plankton biomasses and high mesocale activity. It is clear that horizontal stirring decreases with decreasing latitude. In Fig. 3 (a) we see that, for *Satellite1/4*, the values of FSLEs decay from 0.18 $days^{-1}$ in the southern to 0.03 $days^{-1}$ in the northern area, with similar significant decays for *ROMS1/4* and *ROMS1/12*. Specifically the North-South difference for *Satellite1/4*, *ROMS1/4* and *ROMS1/12* are of the order of 0.15 $days^{-1}$, 0.15 $days^{-1}$ and 0.08 $days^{-1}$, respectively, confirming a lower latitudinal gradient for the case of *ROMS1/12*.

Note that there are differences in the stirring values (FSLEs) depending on the type of data, their resolution, the averaging strip, and the grid size of FSLE computation. In general, considering velocities with the same resolution, the lower values correspond to *Satellite1/4* as compared to *ROMS1/4*. On average, values of stirring from *ROMS1/4*

are larger than those from *ROMS1/12*, whereas we would expect the opposite considering the higher resolution of the latter simulation favoring small scales processes. However, this comparison is hampered by the fact that spatial means of FSLE values are reduced when computing them on grids of higher resolution, because the largest values become increasingly concentrated in thinner lines, a consequence of their multifractal character (Hernández-Carrasco et al., 2011). Indeed, one can not compare consistently two FSLEs field computed on a different resolution, whatever the intrinsic resolution of the velocity field is. The FSLEs computed on a 1/4° grid (black and red lines on Fig. 3) cannot be directly compared to FSLE fields computed on a 1/12° grid (green line Fig. 3) (see Hernández-Carrasco et al. (2011)). Note however that when FSLEs are computed using the *ROMS1/12* and *ROMS1/4* flows but on the same FSLE grid with a fixed resolution of 1/12°, one finds smaller values of FSLEs for the coarser velocity field (*ROMS1/4*) (see green and blue lines in Fig. 3). The effect of reducing the velocity spatial resolution on the FSLE calculations is considered more systematically in Appendix A.1. FSLE values obtained from the same FSLE-grid increase as the resolution of the velocity-grid becomes finer (Fig. A.12) A general observation consistent between all datasets is that horizontal mixing is slightly less intense and more variable in the region of coastal upwelling (from the coast to 3° offshore) than within the transitional area with the open ocean (3-6° offshore). Note also that a low-stirring region is observed within the 3° width coastal strip from 28° to 30°S on all calculations. These observations confirm that the ROMS model is representing well the latitudinal variability of the stirring as measured from FSLE based on satellite data. These preliminary results indicate that Lyapunov exponents and methods could be used as a diagnostic to validate the representation of mesoscale activity in eddy-resolving oceanic models, as suggested recently by Titaud et al. (2011). Overall, the variability of stirring activity in the Benguela derived from the simulated flow fields is in good agreement with the satellite observations.

4.1.2. Simulated phytoplankton concentrations

Evolution of N, P and Z over space and time is obtained by integrating the systems described by Eqs. (8), (9) and (10). The biological model is coupled to the velocity field after the spin-up time needed to reach stability (60 days). Analysing the temporal average of simulated chlorophyll (Fig. 4), we found that coastal regions with high P extend approximately, depending on latitude, between half a degree and two degrees offshore. It is comparable with the pattern obtained from the satellite-derived chlorophyll data (Fig.4 d)). The spatial correlation between averaged simulated and satellite chlorophyll is as follows: $R^2 = 0.85$ for *Satellite1/4* versus *SeaWIFS*; $R^2 = 0.89$ for *ROMS1/4* versus *SeaWIFS* and $R^2 = 0.85$ for *ROMS1/12* versus *SeaWIFS*. Despite the very simple setting of our model, including the parameterization of the coastal upwelling, the distribution of phytoplankton biomass is relatively well simulated in the Benguela area. Note however that our simulated chlorophyll values are about $\simeq$ 3-4 times lower than satellite data. Many biological and physical factors not taken into account in this simple setting could be invoked to explain this offset. Another possible explanation is the low reliability of ocean color data in the optically complex coastal waters (Mélin et al., 2007).

We now examine the latitudinal distribution of P comparing the outputs of the numerical simulations versus the satellite chlorophyll-a over different coastally oriented strips (Fig.5). Simulated P concentrations are higher in the northern than in the southern area of Benguela, in good agreement with the chlorophyll-a data derived from satellite. A common feature is the minimum located just below the Luderitz upwelling cell (28°S), which may be related to the presence of a physical boundary, already studied and named the LUCORC barrier by Shannon et al. (2006) and Lett et al. (2007). The decrease of P concentration is clearly visible in the open ocean region of the *Satellite1/4* case (Fig. 5 b)). Correlations of zonal averages between simulated and satellite chlorophyll-a are poor when considering the whole area (R^2 ranging from 0.1 to 0.5). However, when considering each subsystem (northern and southern) independently, high correlation coefficients are

found for the south Benguela (R^2 around 0.75), but not for the north. This indicates that our simple modelling approach is able to simulate the spatial patterns of chlorophyll in the south Benguela, but not properly in the northern part. In the north, other factors not considered here (such as the 3D flow, the varying shelf width, the external inputs of nutrients, realistic non-climatologic forcings, complex biogeochemical processes, etc...) seem to play an important role in determining the surface chlorophyll-a observed from space.

4.2. Relationship between phytoplankton and horizontal stirring.

In Fig. 6 we show six selected snapshots of chlorophyll concentrations every 8 days during a 32 days period for *ROMS1/12*. Since both ROMS simulations were climatologically forced runs, the dates do not correspond to a specific year. The most relevant feature is the larger value of concentrations near the coast due to the injection of nutrients. Obviously the spatial distribution of P is strongly influenced by the submeso- and meso-scale structures such as filaments and eddies, especially in the southern subsystem. Differences are however observed between the three data sets. In particular, it seems that for *Satellite1/4* and *ROMS1/12* the concentrations extend further offshore than for *ROMS1/4* (not shown). In Appendix A.1 we provide additional analysis of the effect of the velocity spatial resolution on phytoplankton evolution. We found that velocity data with different resolution produces similar phytoplankton patterns but larger absolute values of concentrations as the spatial resolution of the velocity field is refined (see Mahadevan and Archer (2000); Levy et al. (2001)), supporting the need to compare different spatial resolutions.

Several studies (Lehan et al., 2007; d'Ovidio et al., 2009; Calil and Richards, 2010) have shown that transport of chlorophyll distributions in the marine surface is linked to the motion of local maxima or ridges of the FSLEs. This is also observed in our numerical setting when superimposing contours of high values of FSLE (locating the LCSs) on top of phytoplankton concentrations for *ROMS1/12* (see Fig. 6). In some regions P

concentrations are constrained and stirred by lines of FSLE. For instance, the elliptic eddy-like structure at 13 °E, 32 °S is characterized by high phytoplankton concentrations at its edge, but relatively low in its core. This reflects the fact that tracers, even active such as chlorophyll, still disperse along the LCSs.

From Fig. 5 it is clear that phytoplankton biomass has a general tendency to decrease with latitude, an opposite tendency to the one exhibited by stirring (as inferred from the FSLEs and EKE distributions in Figs. 2 and 3) for the three data sets. Moreover, note that the minimum of phytoplankton located just below the LUCORC barrier at 28°S (Fig. 5) coincides with a local maximum of stirring that might be responsible for this barrier (Fig. 3 a). Spatial mean and latitudinal variations of FSLE and chlorophyll-a analyzed together suggest an inverse relationship between those two variables. The 2D vigorous stirring in the south and its associated offshore export seem sufficient to simulate reasonably well the latitudinal patterns of P. The numerous eddies released from the Agulhas system and generally travelling north-westward, associated with the elevated mesoscale activity in the south Benguela, might inhibit the development of P and export unused nutrients toward the open ocean. Although Gruber et al. (2011) invoked the offshore subduction of unused nutrients (3D effect), our results suggest that 2D offshore advection and intense horizontal mixing could by themselves affect negatively the phytoplankton growth in the southern Benguela.

To study quantatively the negative effect of horizontal stirring on phytoplankton concentration, we examine the correlation between the spatial averages – over each subregion (North and South) and the whole area of study – of every weekly map of FSLE and the spatial average of the corresponding weekly map of simulated P, considering each of the three velocity fields (Fig.7). For all cases, a negative correlation between FSLEs and chlorophyll emerges: the higher the surface stirring/mixing, the lower the biomass concentration. The correlation coefficient taking into account the whole area is quite high for all the plots, R^2=0.77 for *Satellite1/4*, 0.70 for *ROMS1/4* and 0.84 for *ROMS1/12* ,

and the slopes (blue lines in Fig.7 have the following values: -1.8 for *Satellite1/4*, -0.8 for *ROMS1/4* and -2.3 for *ROMS1/12*. The strongest negative correlation is found for the setting with *ROMS1/12*. Note that, similarly to the results of Rossi et al. (2008, 2009) and Gruber et al. (2011), the negative slope is larger but less robust when considering the whole area rather than within every subregion. Moreover, if we average over the coastal strip (from coast to 3° offshore) and only in the south region (Fig.7 d),e),f)) we find high values of the correlation coefficient for the *Satellite1/4*, and *ROMS1/12* cases. The suppressive effect of stirring might be dominant only when stirring is intense, as in the south Benguela. Gruber et al. (2011) stated that the reduction of biomass due to eddies may extend beyond the regions of the most intense mesoscale activity, including the offshore areas that we do not simulate in this work.

In the following we analyse the bio-physical mechanisms behind this negative relationship.

4.3. What causes the variable biological responses within regions of distinct dynamical properties?

In the following, our analysis is focused on the setting using *ROMS1/12* as the previous results revealed that the negative correlation is more robust. Similar results and conclusions can be obtained from the simulations using the two other velocity fields (not shown), attesting of the reliability of our approach (see correlation coefficients and slopes in Fig. 7).

To understand why simulated chlorophyll-a concentrations differs in both subsystems, as is the case in satellite observations, we compute annual budgets of N, P, Z and biological rates (Primary Production PP, Grazing and Remineralization) in the case of the biological module alone (Table 2) and when coupled with a realistic flow (Table 3). Considering the biological module alone, we found that PP in the north subsystem is slightly higher than in the southern one (4%, see also Table 2), essentially due to the differential nutrient inputs Φ_N. However, when considering the full coupled system (hydrodynamic and biology), the

latitudinal difference in PP increases significantly (32%, see also Table 3). This latitudinal difference is in agreement with the patterns of PP derived from remote-sensed data by Carr (2002). These results indicate that the flow is the main responsible of the difference in PP. Additional computations (see Appendix A.2) also confirm the minor effect of the biological module (Φ_N), as compared with the flow, on the observed latitudinal differences in PP.

Annual budgets only biological system			
	South	North	North-South difference (%)
Nutrients ($mmolNm^{-3}$)	821	1305	37
Phytoplankton ($mmolNm^{-3}$)	57.0	57.7	1
Zooplankton ($mmolNm^{-3}$)	113	115	2
Primary Production ($mmolNm^{-3}yr^{-1}$)	35	36	4
Grazing ($mmolNm^{-3}yr^{-1}$)	33	35	4
Φ_N ($mmolNm^{-3}yr^{-1}$)	28	29	3
Remineralization ($mmolNm^{-3}yr^{-1}$)	7.0	7.4	4

Table 2: Budgets of N,P,Z and biological rates (Primary Production, Grazing, Φ_N, and remineralization) for the biological model.

Gruber et al. (2011)) suggested that the offshore advection of plankton biomass enhanced by mesoscale structures might be responsible for the suppressive effect of stirring in upwelling areas. To test this mechanism, we next analyze the net horizontal transport of biological tracers by the flow. In particular, we have computed the zonal, JC_ϕ, and meridional, JC_θ, advective fluxes of N, P, Z (the diffusive fluxes being much smaller):

$$JC_\phi(\mathbf{x},t) = u(\mathbf{x},t)C(\mathbf{x},t), \tag{11}$$

$$JC_\theta(\mathbf{x},t) = v(\mathbf{x},t)C(\mathbf{x},t), \tag{12}$$

Annual budgets hydrodynamics-biology coupled system			
	South	North	North-South difference (%)
Nutrients ($mmolNm^{-3}$)	849	1937	56
Phytoplankton ($mmolNm^{-3}$)	147	198	26
Zooplankton ($mmolNm^{-3}$)	231	347	33
Primary Production ($mmolNm^{-3}yr^{-1}$)	63	98	32
Grazing ($mmolNm^{-3}yr^{-1}$)	56	87	35
Φ_N ($mmolNm^{-3}yr^{-1}$)	81	91	10
Remineralization ($mmolNm^{-3}yr^{-1}$)	11	18	4

Table 3: Budgets of N,P,Z and biological rates (Primary Production, Grazing, Φ_N, and remineralization) for the bio-flow coupled model.

where u and v are the zonal and meridional components of the velocity field respectively, and with C we denote the N, P and Z concentrations, all of them given at a specific point in the 2D-space and time $(\mathbf{x}, t)$. JC is the flux of the concentration, C, i.e., JN_ϕ is the zonal flux of nutrients (eastward positive), JP_θ is the meridional flux (northward positive) of phytoplankton, and so on. Annual averages of daily fluxes were computed, and then a zonal average as a function of the latitude was calculated for the different coastal bands considered all along this paper. Fig. 8 shows these calculations for the velocity field from *ROMS1/12*, while similar results were found for the other data sets (not shown). Similar behavior is observed for the fluxes of N, P and Z: zonal fluxes are almost always negative, so that westward transport dominates, and meridional fluxes are predominantly positive so that they are directed to the north. Comparing North and South in the 3° coastal band, it is observed that at high latitudes the zonal flux has larger negative values than at low latitudes, and the meridional flux presents larger positive values at higher latitudes. In other words, the northwestward transport of biological material is more intense in the southern than in the northern regions, suggesting a higher 'flushing rate'. It also suggests

that unused nutrients from the southern Benguela might be advected toward the northern areas, possibly promoting even further the local ecosystem.

To estimate the transport of recently upwelled nutrients by LCSs and other mesoscale structures, apart from the mean flow, we compute the zonal and meridional fluxes of biological tracers using the smoothed *ROMS1/12* velocity field at the spatial resolution equivalent to 1/2° (see Appendix A.1 for more details). The results, plotted in Fig. 8 (red lines), show that in general the fluxes are less intense in the coarser than in the finer velocity, indicating that there is a contribution to net transport due to the submeso- and meso-scale activity. To estimate the quantitative contribution of mesoscale processes, we compute the difference of the fluxes of the different biological tracers $C = N, P, Z$, Q_{JC}, in the coarser velocity field with respect to the original velocity field. The values of Q_{JC} range from 30 to 50%, indicating that the contribution of the mesocale to the net transport of the biological concentrations is important. Moreover, the values of Q_{JC} are larger in the south than in the north confirming that the mesoscale-induced transport is more intense in the south.

Lachkar and Gruber (2011) showed that mesoscale processes reduce the efficiency of nutrients utilization by phytoplankton due to their influence on residence times. The longer residence times (i.e. the less mesoscale activity) seem to favor the accumulation of biomass. To test this effect in our simulations, we compute the residence times (RT), defined as the the time interval that a particle remains in the coastal trip of 5° wide. The spatial distribution (not shown) of the annual average of RT indicates that the longest RT are found in the north region. In fact, zonal analysis reveals that RT has a tendency to increase as the latitude decreases, with a mean value in the North equals to $249 days$, and $146 days$ in the South. This suggests that regions with weak fluxes are associated with long residence times and high growth rate of phytoplankton. On the other hand, high mesoscale activity is favoring the northwestward advection which decreases the residence times, associated to lower growth rate of plankton.

This effect and the role of horizontal advection is confirmed by performing numerical simulations where no biological dynamics is considered. This amounts to solving Eq. (4) with $P = Z = 0$ considering solely lateral transport, so that N is a passive scalar with sources. In Fig. 9 we see the results (for the $ROMS1/12$ case, similar for the other datasets). There is a very small tracer concentration in the southern domain, and the differences north-south are more pronounced than the case including the plankton dynamics (see Fig. 5). This supports further the fact that the main actor on the spatial distribution of biomasses is the horizontal transport.

5. Conclusions

We have studied the biological dynamics in the Benguela area by considering a simple biological NPZ model coupled with different velocity fields (satellite and model). Although in a simple framework, a reduction of phytoplankton concentrations in the coastal upwelling for increasing mesoscale activity has been successfully simulated. Horizontal stirring was estimated by computing the FSLEs and was correlated negatively with chlorophyll stocks. Similar correlations are found, though not presented in this manuscript, for the primary production. Some recent observational and modelling studies proposed the "nutrient leakage" as a mechanism to explain this negative correlation. Here we argue that Lagrangian Coherent Structures, mainly mesoscale eddies and filaments, transport a significant fraction (30-50%) of the recently upwelled nutrients nearshore toward the open ocean before being efficiently used by the pelagic food web. The fluxes of nutrients and organic matter, due to the mean flow and its mesoscale structures, reflect that transport is predominantly westward and northward. Biomass is transported towards open ocean or to the northern area. In addition to the direct effect of transport, primary production is also negatively affected by high levels of turbulence, especially in the south Benguela. Although some studies dealt with 3D effects, we have shown that 2D advection processes seems to play an important role in this suppressive effect. Our analysis suggests that the

inhibiting effect of the mesoscale activity on the plankton occurs when the stirring reaches high levels, as in the south Benguela. However, this effect is not dominant under certain levels of turbulence. It might indicate that planktonic ecosystems in oceanic regions with vigorous mesoscale dynamics can be, as a first approximation, easily modeled just by including a realistic flow field. The small residence times of waters in the productive area will smooth out all the other neglected biological factors in interaction.

Our findings confirm the unexpected role that mesoscale activity has on biogeochemical dynamics in the productive coastal upwelling. Strong vertical velocities are known to be associated with these physical structures and they might have another direct effect by transporting downward rich nutrient waters below the euphotic zone. Further studies are needed such as 3D realistic modelling that take into account the strong vertical dynamics in upwelling regions to test the complete mechanisms involved.

Acknowledgments

I.H-C was supported by a FPI grant from MINECO to visit LEGOS. We acknowledge support from MINECO and FEDER through projects FISICOS (FIS2007-60327) and ESCOLA (CTM2012-39025-C02-01). V. G. thanks CNES funding through Hiresubcolor project. We are also grateful to J. Sudre for providing us velocity data sets both from ROMS and from the combined satellite product. Ocean color data were produced by the SeaWiFS project at GES and were obtained from DAAC.

Appendix A. Sensitivity analysis

A number of numerical experiments were done to investigate the sensitivity of the coupled bio-physical model with respect to different variables.

Appendix A.1. Sensitivity with respect to different spatial resolution of the velocity field

In this experiment we used a velocity field from ROMS1/12 smoothed out towards a resolution 1/4°, and to be compared with $ROMS1/4$ and $ROMS1/12$ at their original

spatial resolution. We coarse-grained the velocity field with a convolution kernel weighted with a local normalization factor, and keeping the original resolution for the data so that land points are equally well described as in the original data. The coarsening kernel with scale factor s, k_s, is defined as:

$$k_s(x,y) = e^{-\frac{(x^2+y^2)}{2s^2}}. \tag{A.1}$$

To avoid spurious energy dump at land points we have introduced a local normalization weight given by the convolution: $k_s(x,y) * M(x,y)$, where $M(x,y)$ is the sea mask. For points far from the land the weight is just the normalization of k_s, and for points surrounded by land the weight takes the contribution from sea points only. Thus v_s, the velocity field coarsened by a scale factor s, is obtained from the original velocity field v as:

$$v_s = \frac{k_s * v}{k_s * M}. \tag{A.2}$$

In Fig. A.10 we compare two *ROMS1/12* smoothed velocity fields at scales s=3 and s=6 (with an equivalent spatial resolution 1/4° and 1/2°, respectively) with the original velocity field from *ROMS1/12*. It is clear that the circulation pattern is smoothed as s is increased. The FSLE computations using these smoothed velocity fields are shown in Fig A.11. When the spatial resolution is reduced to 1/4° the FSLEs and small-scale contributions decrease, but the main global features remain, as indicated in the study by Hernández-Carrasco et al. (2011). Further coarsening to 1/2° smoothes most of the structures except the most intense ones.

The latitudinal variations of the zonal averages performed on the time averages of the FSLE maps plotted in Fig. A.11 are compared in Fig.A.12. The mean FSLEs values strongly diminish when the velocity resolution is sufficiently smoothed out. This is due to the progressive elimination of mesoscale structures that are the main contributors to stirring processes. Also the latitudinal variability of stirring diminishes for the very

smoothed velocity field (blue line in Fig. A.12). Thus, latitudinal differences of stirring in the Benguela system are likely to be related to mesoscale structures (eddies, filaments, fronts, etc.) contained in the velocity fields.

We have also computed the phytoplankton using these smoothed velocity fields. Some instantaneous spatial distributions can be seen in Fig A.13. The filaments of phytoplankton disappear in the very smoothed velocity field ($1/2^{\circ}$). The spatial distribution of the annual average of phytoplankton concentrations for the different velocity field shows, however, quite similar patterns (not shown).

In the time series of N, P and Z budgets for the coarser velocities one observes the same behavior as for the original velocity field (not shown).

Appendix A.2. Sensitivity with respect to different parameterization of the coastal upwelling of nutrients.

In section 3.2 we mimicked coastal upwelling of nutrient via a source term in the nutrients equation which is determined by the function S, and was considered spatiotemporally variable. Here we explore the plankton dynamics using spatially and temporally homogeneous upwelling along the coast. S is fixed to an average value $S = 0.1\ day^{-1}$ along the coast at any time. In Fig. A.14 we show the annual average of P for the $ROMS1/12$ (top panel), and the comparisons with the inhomogeneous case for the zonal mean (bottom panel). Therefore, this test suggests that the way we simulate vertical mixing along the coast has not a large effect on the 2D biological dynamics, which will be mainly determined by the interplay with horizontal advection.

References

Artale, V., Boffetta, G., Celani, A., Cencini, M., Vulpiani, A., 1997. Dispersion of passive tracers in closed basins: Beyond the diffusion coefficient. Phys. Fluids 9, 3162–3171.

Aurell, E., Boffetta, G., Crisanti, A., Paladin, G., Vulpiani, A., 1997. Predictability in the large: an extension of the Lyapunov exponent. J. Phys. A 30, 1–26.

572 Boffetta, G., Lacorata, G., Redaelli, G., Vulpiani, A., 2001. Detecting barriers to trans-
573 port: a review of different techniques. Physica D 159, 58–70.

574 Brink, K., Cowles, T., 1991. The coastal transition zone program. J. Geophys. Res 14,
575 637–647.

576 Calil, P., Richards, K., 2010. Transient upwelling hot spots in the oligotrophic North
577 Pacific. J. Geophys. Res 115, C02003.

578 Carr, M. E., 2002. Estimation of potential productivity in Eastern Boundary Currents
579 using remote sensing. Deep-Sea Res. II 49, 5980.

580 Condie, S., Dunn, J. R., 2006. Seasonal characteristics of the surface mixed layer in the
581 Australasian region: implications for primary production regimes and biogeography
582 Marine and Freshwater Research. Marine and Freshwater Research 57, 1–22.

583 Correa-Ramirez, M., Hormazabal, S., Yuras, G., 2007. Mesoscale eddies and high choro-
584 phyll concentrations off central Chile (29°S - 39°S). Geophys. Res. Lett 34, L12604.

585 Demarcq, H., Barlow, R., Shillington, F., 2003. Climatology and variability of sea sur-
586 face temperature and surface chlorophyll in the Benguela and Agulhas ecosystems as
587 observed by satellite. African Journal of Marine Science 25, 363–372.

588 Doney, S.C., D. G. R. N., 1996. A new coupled, one-dimensional biologicalphysical model
589 for the upper oceanapplication to the JGOFS Bermuda Atlantic Time-series Study
590 (BATS) site. Deep-Sea Res. II 43, 591–624.

591 d'Ovidio, F., Fernández, V., Hernández-García, E., López, C., 2004. Mixing structures
592 in the Mediterranean sea from finite-size Lyapunov exponents. Geophys. Res. Lett. 31,
593 L17203.

d'Ovidio, F., Isern-Fontanet, J., López, C., Hernández-García, E., García-Ladona, E., 2009. Comparison between Eulerian diagnostics and Finite-Size Lyapunov Exponents computed from altimetry in the Algerian basin. Deep-Sea Res. I 56, 15–31.

Gruber, N., Lachkar, Z., Frenzel, H., Marchesiello, P., Münnich, M., McWilliams, J., Nagai, T., Plattner, G., 2011. Eddy-induced reduction of biological production in eastern boundary upwelling systems. Nature Geoscience 9, 787–792.

Gutknecht, E., Dadou, I., Cambon, B. L. V. G., Sudre, J., Garçon, V., Machu, E., Rixen, T., Kock, A., Flohr, A., Paulmier, A., Lavik, G., 2013. Coupled physical/biogeochemical modeling including 02-dependent processes in the Eastern Boundary Upwelling Systems: application in the Benguela. Biogeosciences 10, 3559–3591.

Haller, G., Yuan, G., 2000. Lagrangian coherent structures and mixing in two-dimensional turbulence. Physica D 147, 352–370.

Hernández-Carrasco, I., López, C., Hernández-García, E., Turiel, A., 2011. How reliable are finite-size Lyapunov exponents for the assesment of ocean dynamics? Ocean Modelling 36(3-4), 208–218.

Hernández-Carrasco, I., López, C., Hernández-García, E., Turiel, A., 2012. Seasonal and regional characterization of horizontal stirring in the global ocean. J. Geophys. Res. 117, in press.

Hurtt, G. C., Armstrong, R. A., 1996. A pelagic ecosystem model calibrated with BATS dat. Deep-Sea Res. II 43(2-3), 653–683.

Hutchings, L., van der Lingen, C., Shannon L.J. Crawford, R., Verheye, H., Bartholomae, C., van der Plas, A., Louw, D., Kreiner, A., Ostrowski, M., Fidel, Q., Barlow, R., Lamont, T., Coetzee, J., Shillington, F., Veitch, J., Currie, J., Monteiro, P., 2009. The Benguela Current: An ecosystem of four components. Progress in Oceanography 83, 15–32.

Joseph, B., Legras, B., 2002. Relation between Kinematic Boundaries, Stirring, and Barriers for the Antartic Polar Vortex. J. Atm. Sci. 59, 1198–1212.

Koh, T., Legras, B., 2002. Hyperbolic lines and the stratospheric Polar vortex. Chaos 12 (2), 382–394.

Koné, V., Machu, E., Penven, P., Andersen, V., Garçon, V., Fréon, P., Demarcq, H., 2005. Modeling the primary and secundary productions of the southern Benguela upwelling system: A comparative study through two biogeochemical models. Global Biogeochem. Cycles 19, GB4021.

Lachkar, Z., Gruber, N., 2011. What controls biological production in coastal upwelling systems? Insights from a comparative modeling study. Biogeosciences 8, 2961–2976.

Lehan, Y., d'Ovidio, F., Lévy, M., Heyfetz, E., 2007. Stirring of the Northeast Atlantic spring bloom: A Lagrangian analysis based on multisatellite data. J. Geophys. Res. 112, C08005.

Lett, C., Veitch, J., van der Lingen, C., Hutchings, L., 2007. Assessment of an environmental barrier to transport of ichthyoplankton from the southern to the northern Benguela ecosystems. Marine Ecology Progress Series 347, 247–259.

Levy, M., Klein, P., Treguier, A., 2001. Impact of sub-mesoscale physics on production and subduction of phytoplankton in an oligotrophic regime. J. Mar. Res. 59, 535–565.

Mackas, D., Strub, P., Thomas, C., Montecino., V., 2006. Eastern ocean boundaries pan-regional view. In: Robinson, A., Brink, K. (Eds.), The Sea, vol 14a, The global Coastal Ocean: Interdisciplinary Regional Studies and Syntheses: Pan-Regional Syntheses and the Coast of North and South America and Asia. Harvard Univ. Press, chap. 2, Cambridge, Mass.

642 MacKiver, W., Neufeld, Z., 2009. The influence of turbulent advection on a phytoplankton
643 ecosystem with non-uniform carrying capacity. Phys. Rev. E. 79, 061902.

644 Mahadevan, A., Archer, D., 2000. Modeling the impact of fronts and mesoscale circulation
645 on the nutrient supply and biogeochemistry of the upper ocean. J. Geophys. Res 105,
646 1209–1225.

647 Martin, A., 2003. Phytoplankton patchiness: the role of lateral stirring and mixing.
648 Progress in Oceanography 57, 125–174.

649 McGillicuddy, D., Anderson, N., Bates, T., Buesseler, K., 2007. Eddy/wind interactions
650 stimulate extraordinary mid-ocean plankton blooms. Science 316, 1021–1026.

651 Mélin, F., Zibordi, G., Berthon, J., 2007. Assessment of satellite ocean color products at
652 a coastal site. Remote Sensing Environ 110(2), 192.

653 Monteiro, P., 2009. Carbon fluxes in the Benguela upwelling system. In: Liu, K., Atkin-
654 son, L., Quiñones, R., Talaue-McManus, L. (Eds.), Carbon and Nutrient Fluxes in
655 Continental Margins: A global Synthesis, Chap. 2. Springer, Berlin.

656 Neufeld, Z., Hernández-García, E., 2009. Chemical and Biological Processes in Fluid
657 Flows. A dynamical systems approach. Imperial College, London.

658 Okubo, A., 1971. Oceanic diffusion diagrams. Deep-Sea Res. 18, 789–802.

659 Oschlies, A., Garçon, V., 1998. Eddy-induced enhancement of primary productivity in a
660 model of the North Atlantic Ocean. Nature 394, 266–269.

661 Oschlies, A., Garçon, V., 1999. An eddy-permitting coupled physical-biological model of
662 the North Atlantic, sensitivity to advection numerics and mixed layer physics. Global
663 Biocheochem. Cycles 13, 135–160.

Pasquero, C., Bracco, A., Provenzale, A., 2004. Coherent vortices, Lagrangian particles and the marine ecosystem. In: Uijttewaal, W., Jirka, G. (Eds.), Shallow Flows. Balkema, Leiden.

Rossi, V., López, C., Hernández-García, E., Sudre, J., Garçon, V., Morel, Y., 2009. Surface mixing and biological activity in the four Eastern Boundary Upwellings Systems. Nonlinear Process. Geophys. 16, 557–568.

Rossi, V., López, C., Sudre, J., Hernández-García, E., Garçon, V., 2008. Comparative study of mixing and biological activity of the Benguela and Canary upwelling systems. Geophys. Res. Lett. 35, L11602.

Sandulescu, M., Hernández-García, E., López, C., Feudel, U., 2007. Plankton blooms in vortices: the role of biological and hydrodynamics timescales. Nonlinear Process. Geophys. 14, 443–454.

Sandulescu, M., López, C., Hernández-García, E., Feudel, U., 2008. Biological activity in the wake of an island close to a coastal upwelling. Ecological Complexity 5, 228–237.

Shannon, L., Hempel, G., Malanotte-Rizzoli, P., Moloney, C., Woods, J. (Eds.), 2006. Benguela: Predicting a Large Marine Ecosystem. Elsevier.

Sudre, J., Morrow, R., 2008. Global surface currents: a high resolution product for investigating ocean dynamics. Ocean Dyn. 58(2), 101–118.

Tél, T., de Moura, A., Grebogi, C., Károlyi, G., 2005. Chemical and biological activity in open flows: A dynamical system approach. Physics Reports 413, 91–196.

Tew Kai, E., Rossi, V., Sudre, J., Weimerskirch, H., López, C., Hernández-García, E., Marsac, F., Garçon, V., 2009. Top marine predators track Lagrangian coherent structures. Proceedings of the National Academy of Sciencies of the USA 106, 8245–8250.

687 Titaud, O., Brankart, J. M., Verron, J., 2011. On the use of Finite-Time Lyapunov
688 Exponents and Vectors for direct assimilation of tracer images into ocean models. Tellus
689 A 63, 1038–1051.

690 Veitch, J., Penven, P., Shillington, F., 2009. The Benguela: A laboratory for a comparative
691 modeling studies. Progress in Oceanography 83(1-4), 296–302.

692 Waugh, D. W., Abraham, E. R., 2008. Stirring in the global surface ocean. Geophys. Res.
693 Lett. 35, L20605.

694 Waugh, D. W., Abraham, E. R., Bowen, M. M., 2006. Spatial variations of stirring in the
695 surface ocean: A case of study of the Tasman sea. J. Phys. Oceanogr. 36, 526–542.

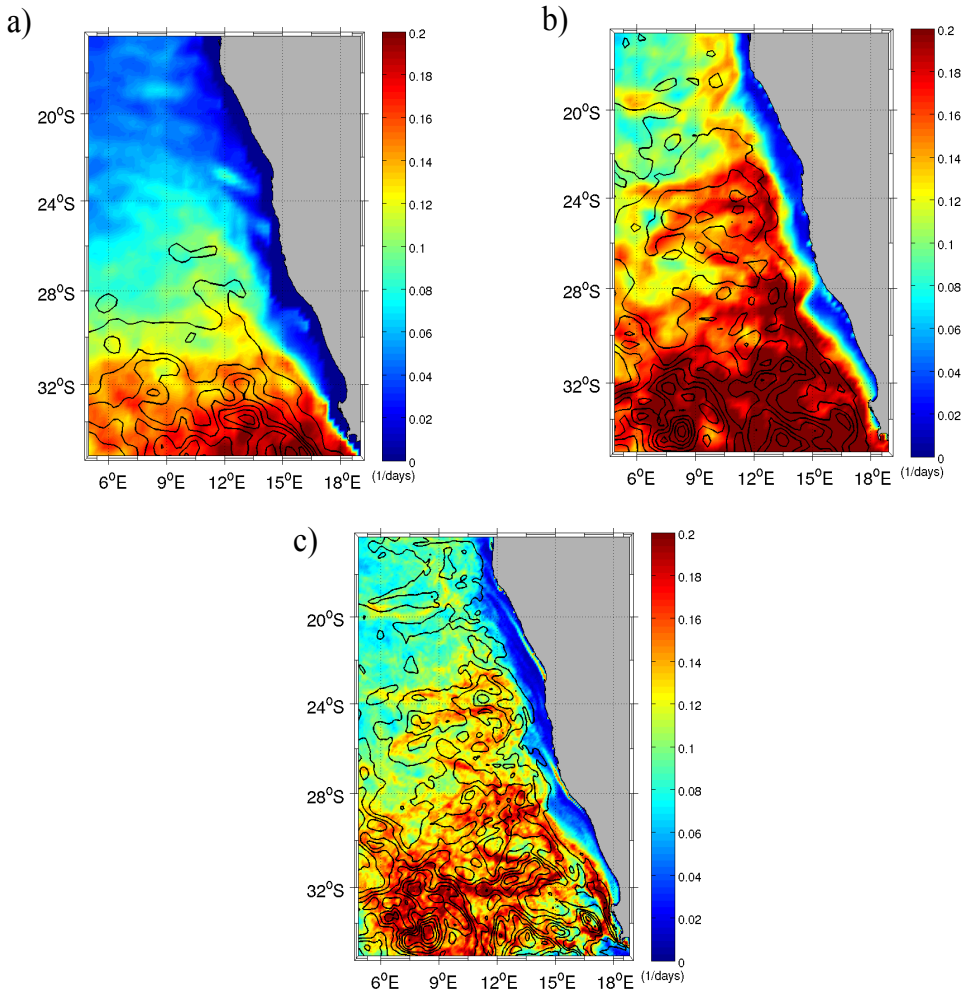

Figure 2: Spatial distribution of time average of weekly FSLE maps in the Benguela region. a) Three years average using data set *Satellite1/4*; b) one year average using *ROMS1/4*; c) one year average using *ROMS1/12*. The units of the colorbar are $1/days$. The black lines are contours of annual EKE. The separation between contour levels is $100cm^2/s^2$.

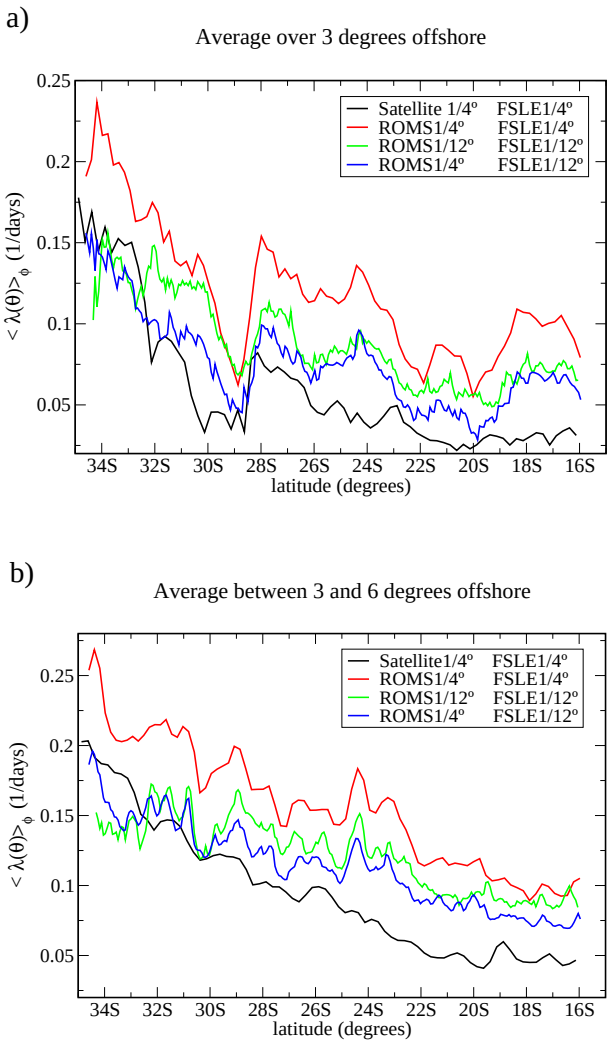

Figure 3: Zonal average on coastal bands of the FSLE time averages from Fig. 2 as a function of latitude. a) from the coast to 3 degrees offshore; b) between 3 and 6 degrees offshore.

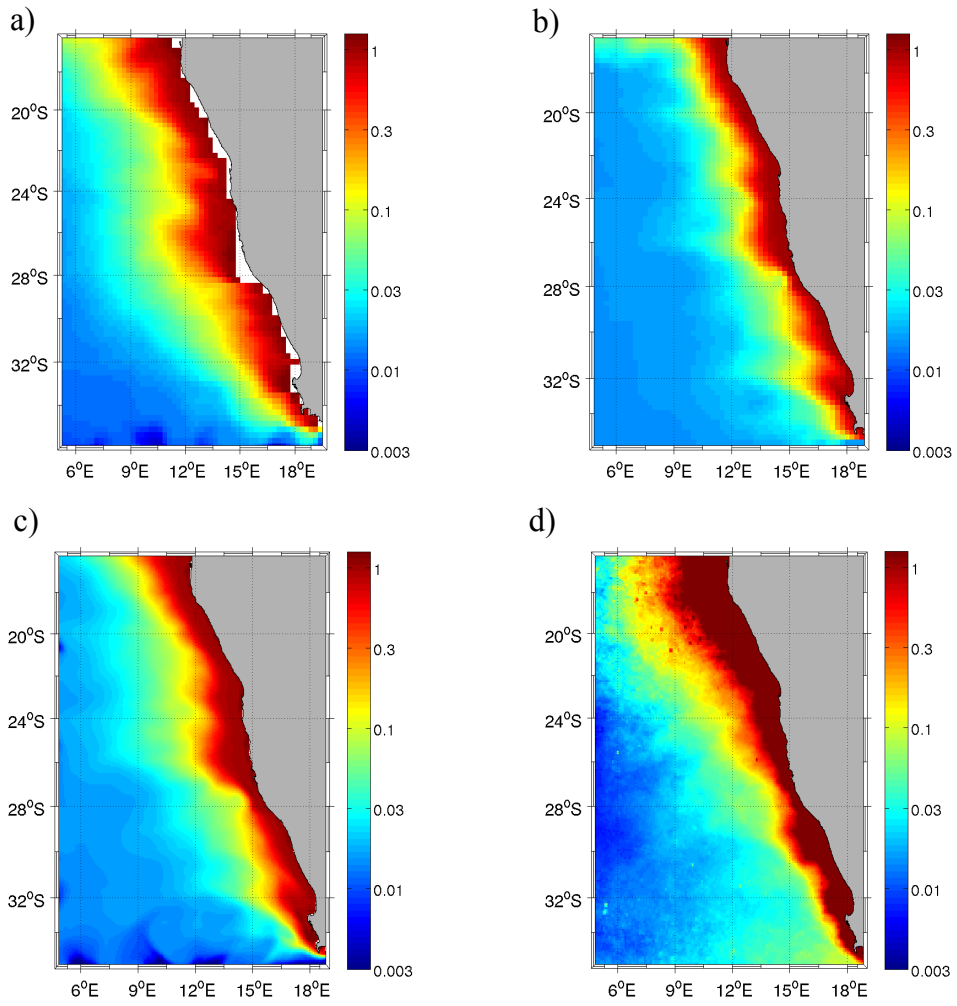

Figure 4: Spatial distribution of: a) Three years average of simulated chlorophyll using *Satellite1/4*, b) One year average of simulated chlorophyll using *ROMS1/4*, c) Same than b) but using *ROMS1/12*, d) Three years average of observed chlorophyll derived from monthly SeaWIFS data. The units of the colorbar are mg/m^3. Logarithmic scale is used to improve the visualization of gradients in nearshore area.

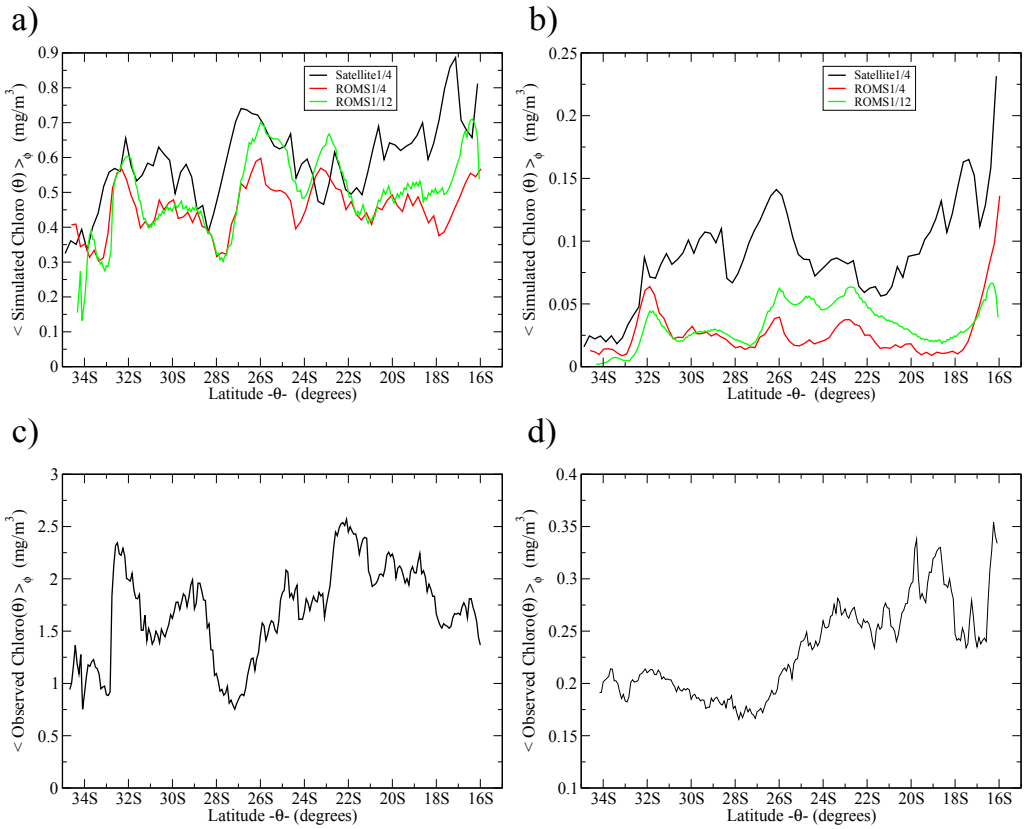

Figure 5: Zonal mean of simulated chlorophyll on a coastally oriented strip from the coast to 3 degrees (a) and from 3 degrees to 6 degrees offshore (b), plotted as a function of latitude. Zonal average of observed chlorophyll (SeaWIFS) over a coastal band from the coast to 3 degrees (c) and from 3 degrees to 6 degrees offshore (d).

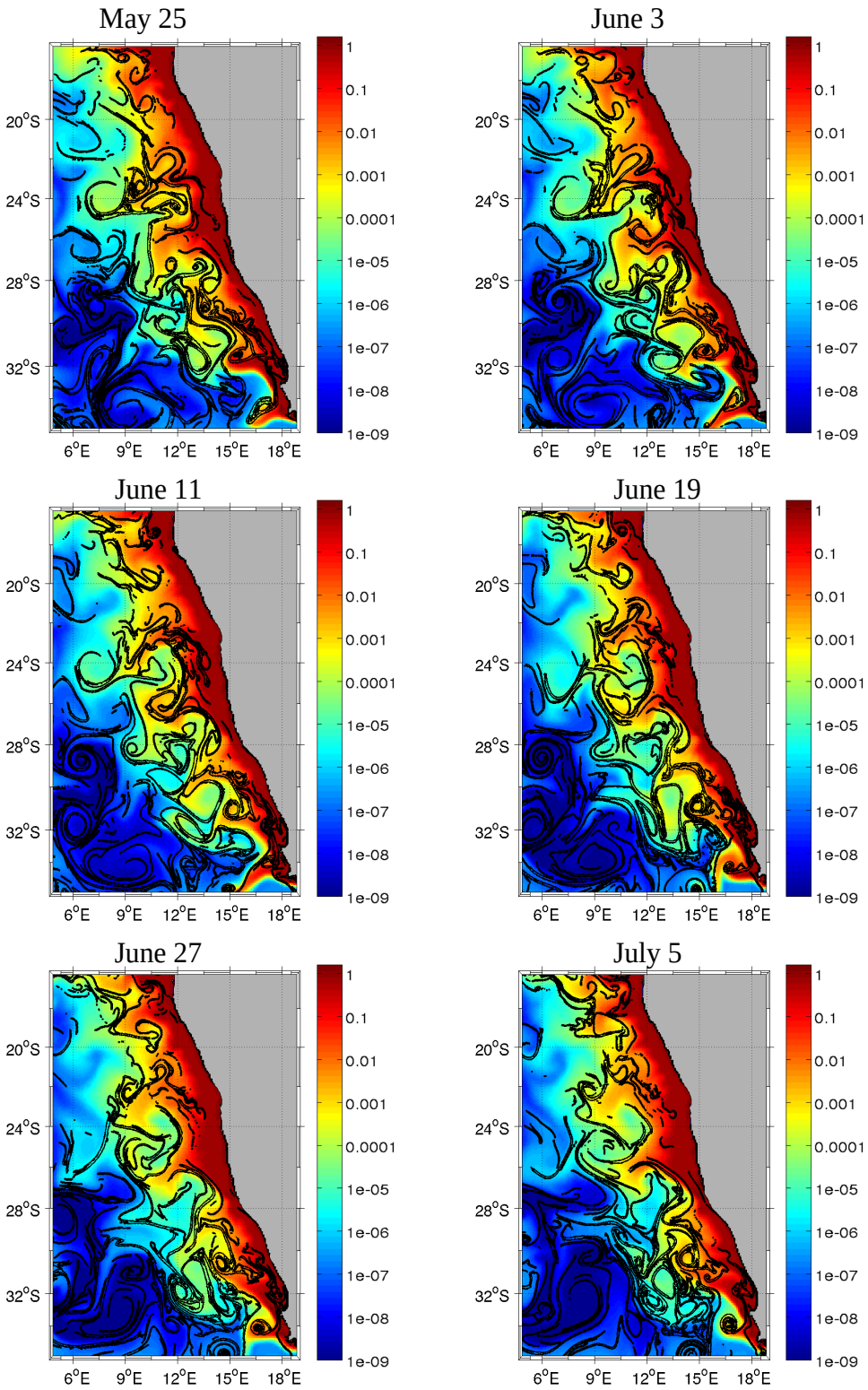

Figure 6: Snapshots every 8 days of large (top 30%) values of FSLE superimposed on simulated chlorophyll concentrations calculated from *ROMS1/12* in mg/m^3. Logarithmic scale for chlorophyll concentrations is used to improve the visualization of the structures

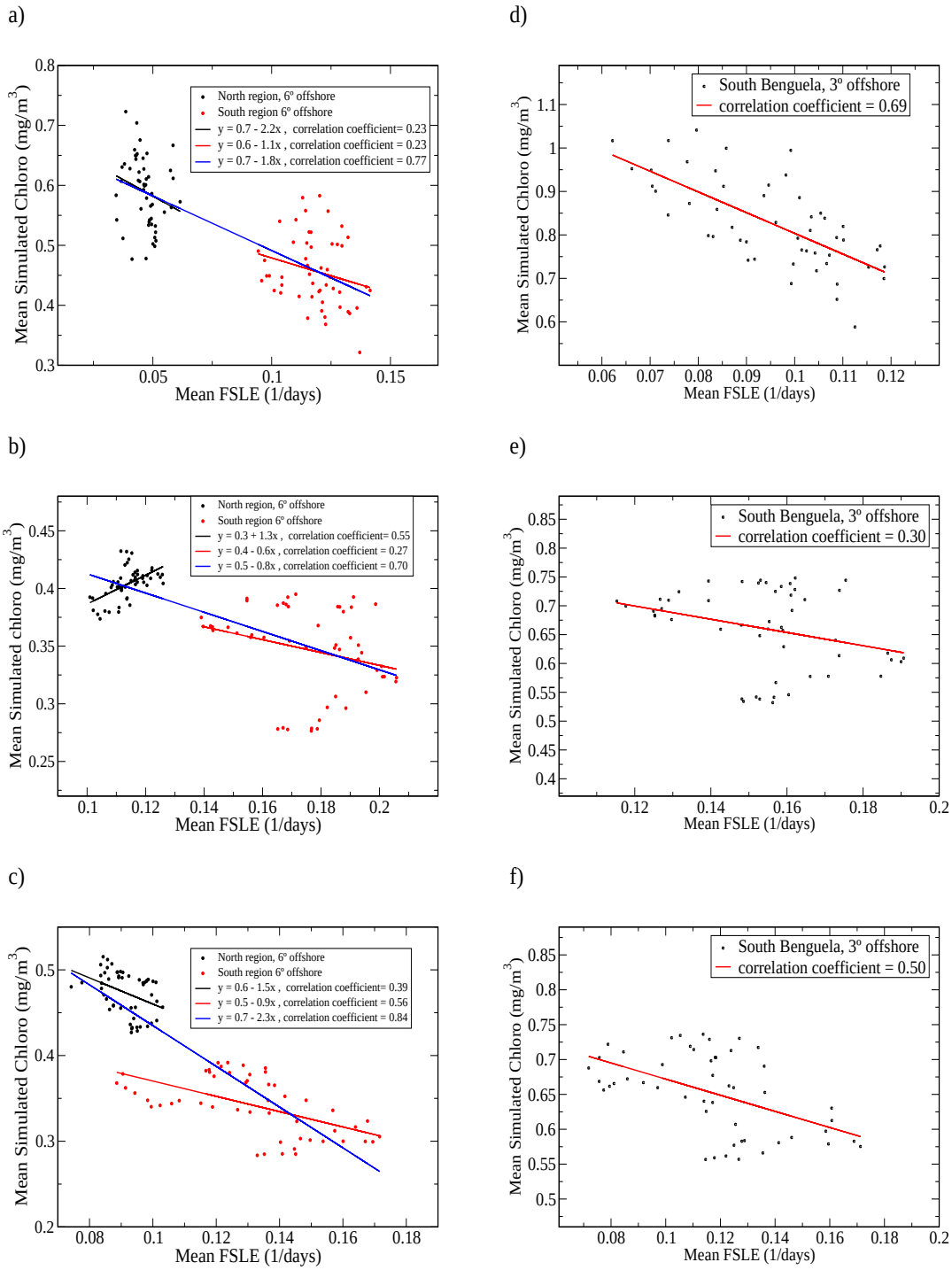

Figure 7: Weekly values of spatial averages of simulated chlorophyll versus weekly values of spatial averages of FSLE, where the average are over the whole area (6 ° from the coast) and in North and South subareas of Benguela. a) *Satellite1/4*, b) *ROMS1/4* and c) *ROMS1/12*. Right column plots the average over 3° offshore in the south region: d) *Satellite1/4*, e) *ROMS1/4* and f) *ROMS1/12*

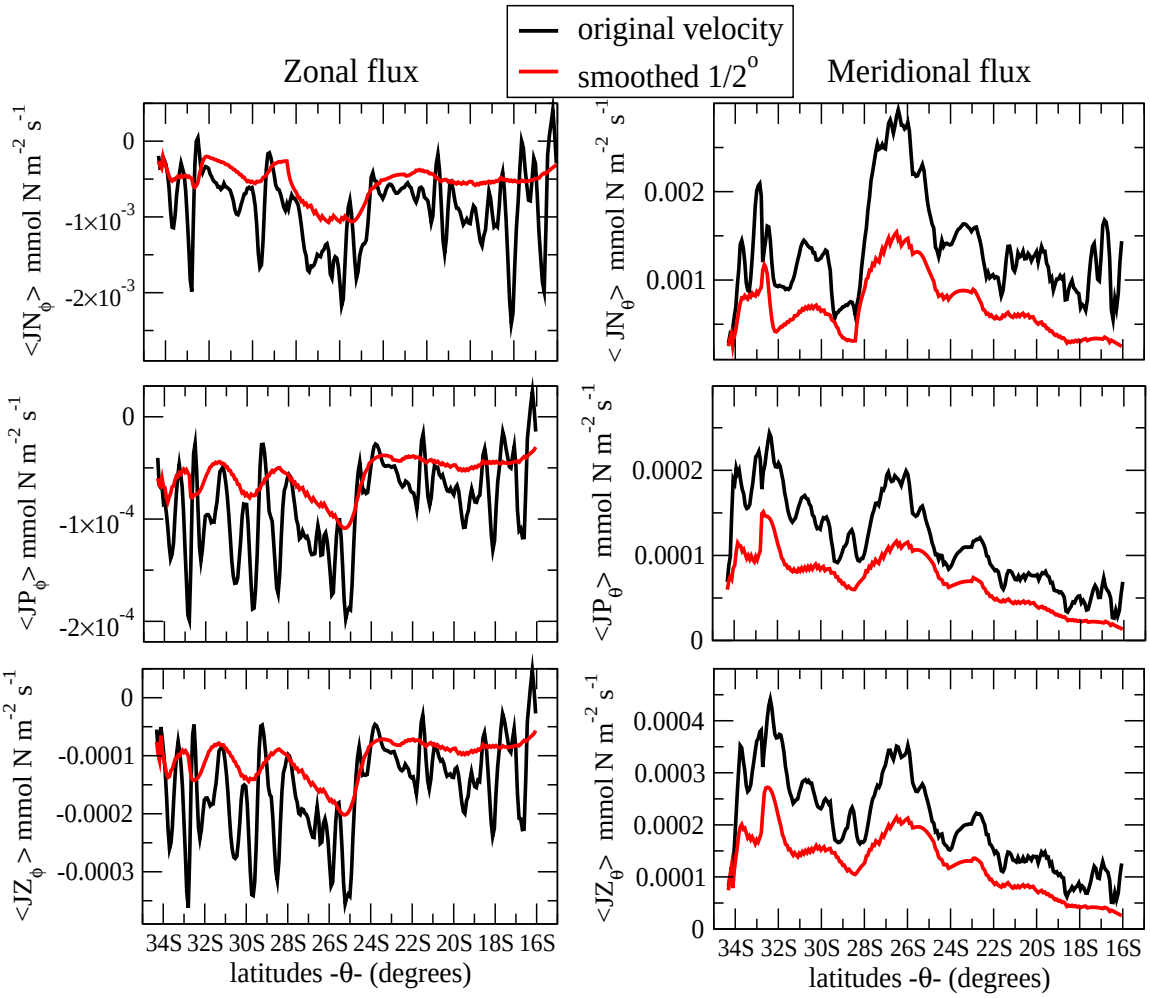

Figure 8: Zonal mean of zonal and meridional fluxes of N, P, Z concentrations for the *ROMS1/12* case, averaged from the coast to 3° offshore.

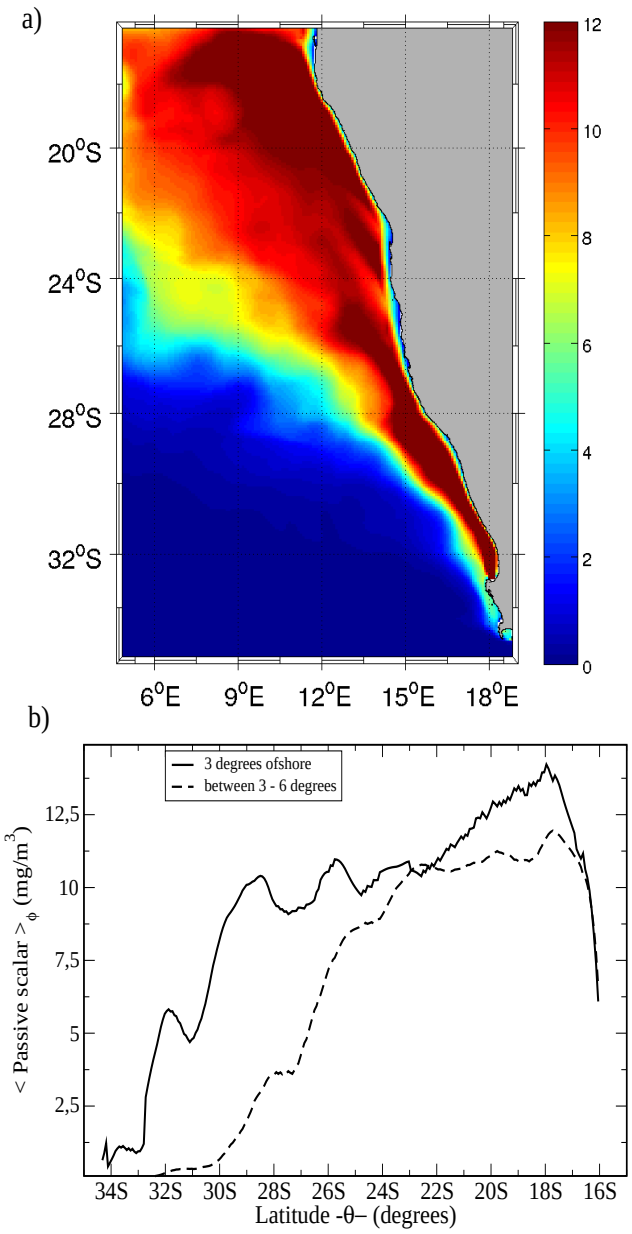

Figure 9: a) Spatial distribution of time average of the passive scalar concentration (see details at the end of subsection 4.3). b) Comparison of latitudinal profile of time averages of the passive scalar, as a function of latitude, for zonal average over different coastal bands.

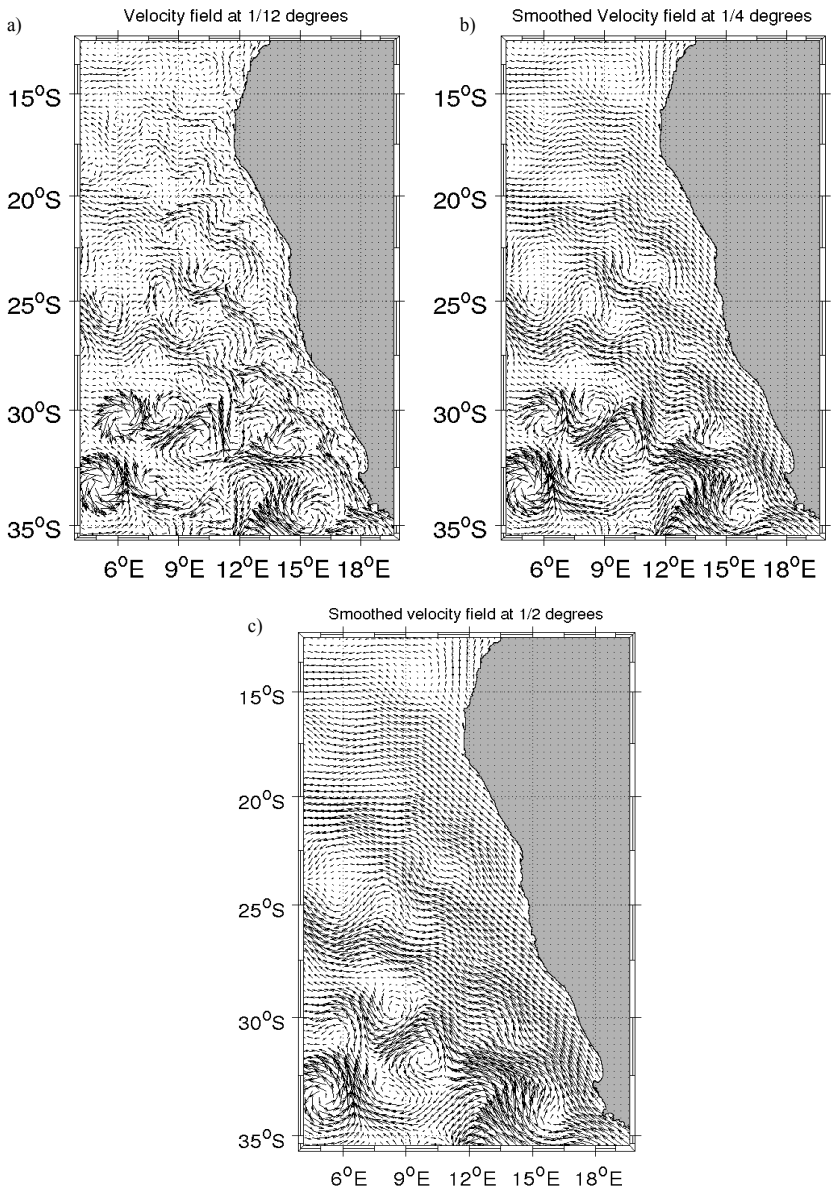

Figure A.10: Vectors of a velocity field from $ROMS1/12$: a) at original resolution. b) smoothed by a scale factor of s=3, obtaining and equivalent spatial resolution of 1/4°, c) smoothed by a scale factor of s=6, obtaining and equivalent spatial resolution of 1/2°. The snapshots correspond to day 437 of the simulation.

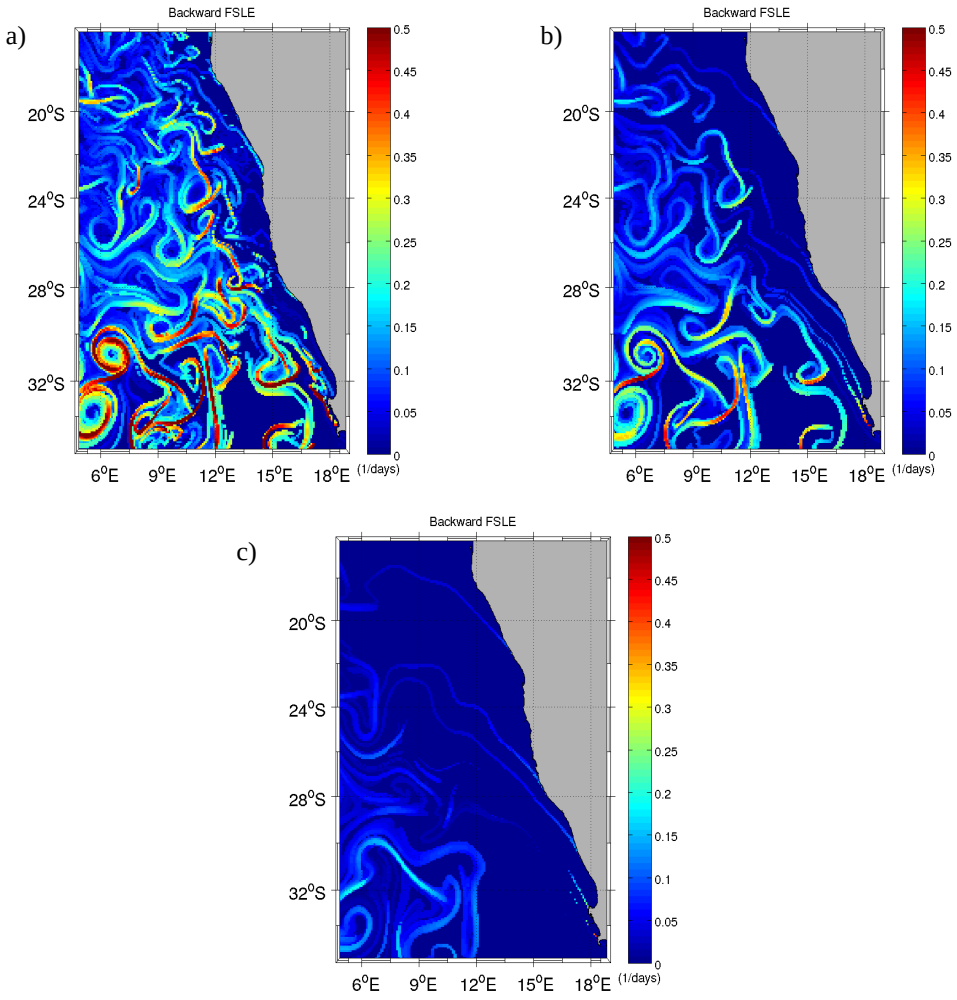

Figure A.11: Snapshots of spatial distributions of FSLEs backward 437 days in time starting from day 437 of $ROMS1/12$ at the same FSLE grid resolution of $1/12°$, and using the velocity fields at different resolutions: a) at original resolution $1/12°$. b) smoothed velocity field at equivalent $1/4°$ and c) smoothed velocity field at equivalent $1/2°$.

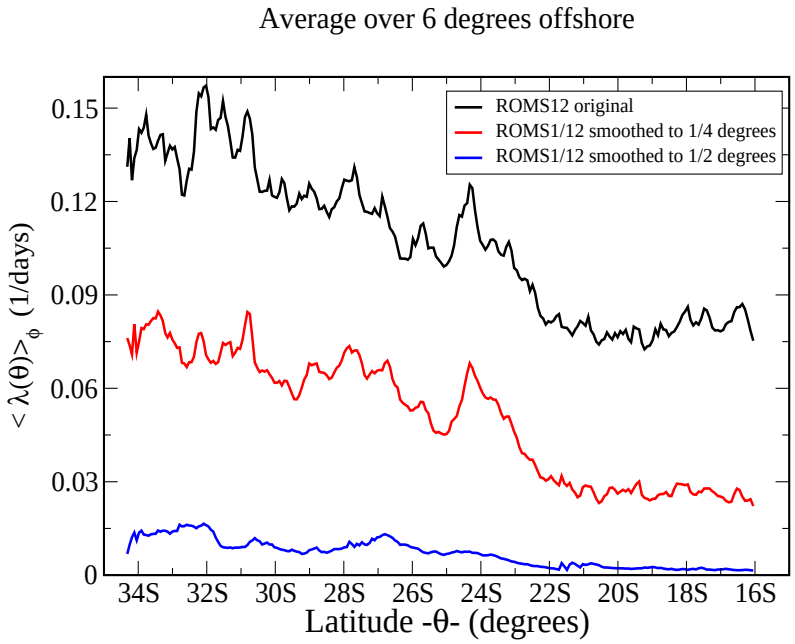

Figure A.12: Latitudinal profile of the zonal mean values of annual averaged backward FSLEs (51 snapshots weekly separated) at the same FSLE grid resolution of 1/12°, and using different smoothed velocity fields.

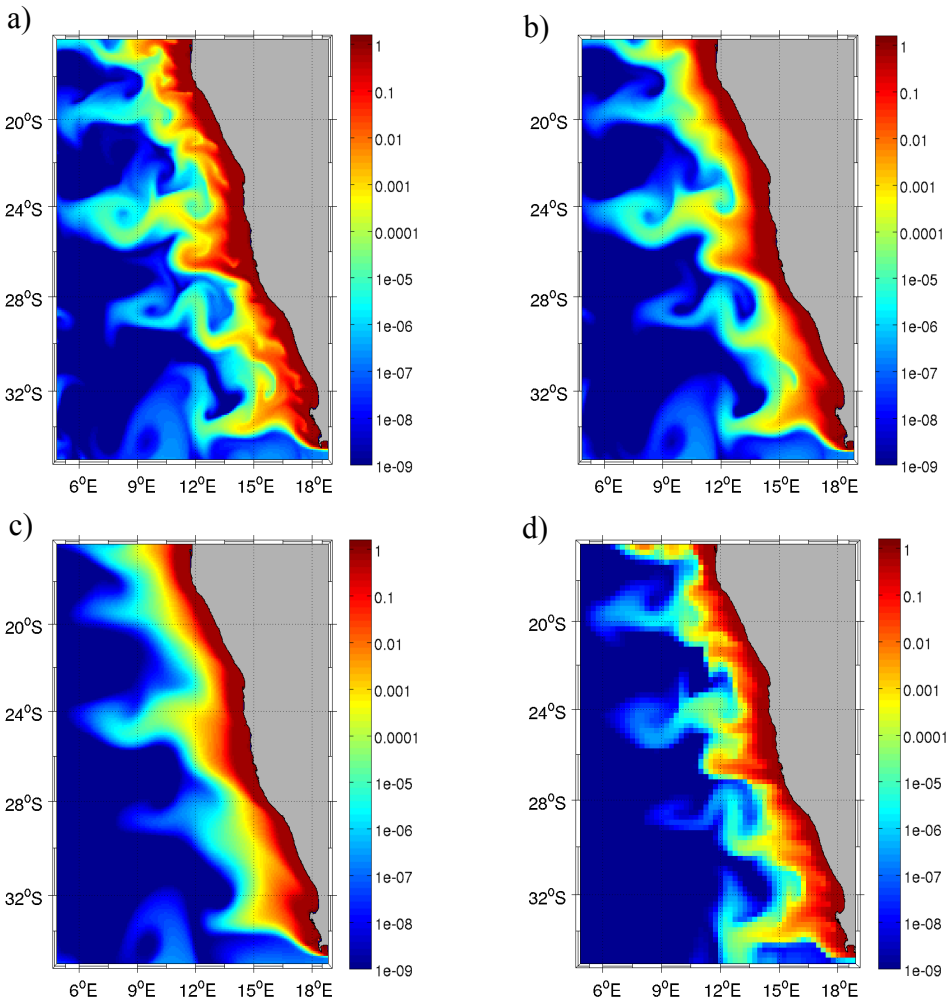

Figure A.13: Snapshots of simulated chlorophyll field using different velocity fields: a) $ROMS1/12$ at original resolution $1/12°$, b) smoothed $ROMS1/12$ velocity field at equivalent $1/4°$, c) smoothed $ROMS1/12$ velocity field at equivalent $1/2°$, and d) $ROMS1/4$ at original resolution $1/4°$. The units of the colorbar are mg/m^3.

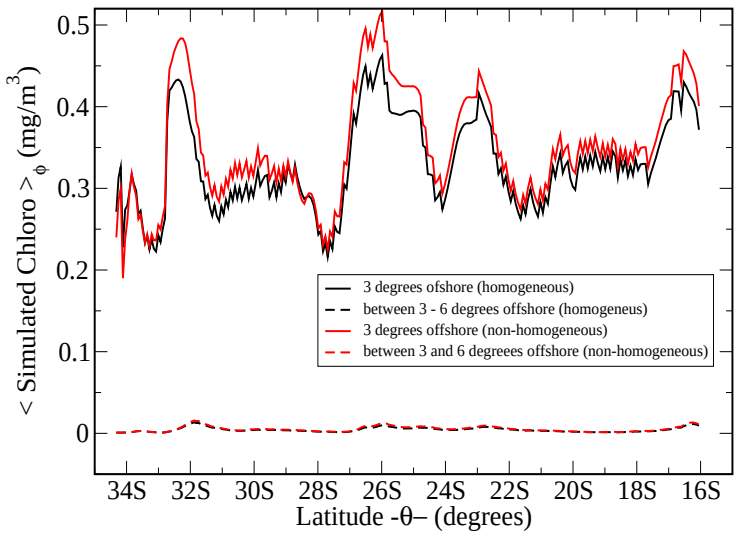

Figure A.14: Comparison between zonal average on different coastal bands of annual time average of simulated chlorophyll, using homogeneous upwelling and the non-homogeneous upwelling cells described in Fig. 1.